Modeling and satellite observations of baroclinic tidal flows and inundation processes in Cook Inlet, Alaska

Lie-Yauw Oey and Tal Ezer
Princeton University
Program in Atmospheric and Oceanic Sciences
P.O.Box CN710, Sayre Hall
Princeton, NJ 08544-0710, USA

Chuanmin Hu and Frank E. Muller-Karger
University of South Florida
College of Marine Science, Institute for Marine Remote Sensing
St. Petersburg, FL 33701, USA

Communicating author: T. Ezer,
Email: ezer@splash.princeton.edu
Tel: +1-609-2581318
Fax: +1-609-2582850

Submitted to *Ocean Dynamics*: 7 September, 2006

Abstract: A Wetting and Drying (WAD) algorithm is implemented in a baroclinic three-dimensional ocean circulation model of the Cook Inlet, Alaska, where large tidal ranges (≈ 10 meters) regularly expose extensive mud flats. The model includes tides and wind- and buoyancy-induced flows. In the Upper Inlet the model successfully simulates large amplification of tides and propagation of fast (3~4 m s^{-1}) tidal bores over shallow mud flats. The simulated return flows during ebb expose large areas (~100 km^2) of the mud flats. Medium-resolution (250- and 500-m) images obtained from the MODerate resolution Imaging Spectroradiometer (MODIS) instruments aboard the Terra and Aqua satellites were used to verify the model results by identifying the location, extent and temporal changes of exposed mud flat regions. The results demonstrate the value of operational, medium-resolution remote sensing data in evaluating the WAD model. Sensitivity tests show that WAD produces approximately *20%* larger tidal amplitude and *10%* slower phase than the corresponding experiment without WAD. In the deep channel of the Central Inlet, confluence of saline water of the lower Inlet with brackish water from rivers and melting ice from land around the upper Inlet produces a salinity front. At the simulated front, strong vertical circulation cells and surface convergence and currents develop, especially during the flood. These resemble "rip tides" often observed in this region.

Keywords: numerical model, tides, inundation, satellite data, MODIS, Alaska

1. Introduction

Wetting and drying (WAD) is a common and important phenomenon of the coastal ocean and estuaries, especially over low-lying coastal zones. In bays and inlets with large-amplitude tides, such as in the Bay of Fundy (Gulf of Maine) and the Cook Inlet (Alaska), WAD is an essential part of the local environment and ecosystem. In extreme cases, effects of WAD are dramatic and tragic, as demonstrated recently during the Indian Ocean tsunami (December, 2004) and the flooding of New Orleans by Hurricane Katrina (August, 2005). WAD modeling is clearly of practical importance, but until recently WAD schemes have been implemented mostly in hydraulic and in coastal/estuarine models (Stelling et al. 1986; Balzano 1998; Lynch and Grey 1980; Flather and Hubbert 1990; Casulli and Cheng 1992; Lin and Falconer 1997; Ji et al. 2001; Xie et al. 2003; Chen et al. 2006). However, as various regional and large-scale ocean general circulation models (OGCM's) and forecast systems evolve (Chassignet et al., 2003; Drillet et al., 2005; Ezer and Mellor, 2000; Fan et al., 2004; Ko et al., 2003; Marchesiello et al., 2003; Romanou et al., 2004; Sheng and Tang, 2003; Smith et al., 2000; and Oey et al., 2003; 2005), the distinction between the coast and open ocean becomes blurred, and there is a need to include dynamic (or movable) coastal boundaries to model inundation processes. The first such OGCM using the Princeton Ocean Model (POM; Blumberg and Mellor 1987; Mellor 2004) has recently been developed and described in Oey (2005, 2006). In these latter papers, idealized one-, two- and three-dimensional cases such as the dam-break, "water fall," tsunami, tidal, and estuarine-circulation problems were tested. The POM-WAD implementations rely on the vast experiences of coastal and estuarine modelers (cited above), but are unique in two

important ways. Firstly, the WAD algorithm is implemented in a three-dimensional baroclinic ocean forecast system that is equipped with data assimilative tools, nesting capabilities and large-scale and regional forcing (see http://www.aos.princeton.edu/WWWPUBLIC/PROFS/ and publications listed therein). Secondly, the WAD conditions across cells' interfaces are fully dynamic using the full set of primitive equations. In this paper, we describe the model implementations and results for the Cook Inlet, Alaska, where tidal range reaches 10 meters and active WAD physics exist. Combined with the availability of repeated medium-resolution remote sensing imagery, we will also attempt to evaluate the simulated WAD processes.

Cook Inlet, Alaska, is named after the English explorer James Cook (1728-1779) who in 1778 sailed along the northwestern coast of North America and the Bering Strait (Beaglehole, 1974). The Inlet extends approximately 250~300 km from the Gulf of Alaska in the south into the city of Anchorage in the northeast where it branches into two shallower extensions, the Knik Arm north of Anchorage and the Turnagain Arm southeast of Anchorage (Fig.1). Water levels and currents in Cook Inlet are strongly influenced by tides from the Gulf of Alaska. The 'tidal resonant' length scale can be estimated by $(gH_{ave})^{1/2}P/4 \approx 250$ km (Gill, 1982), where $g = 9.8$ m s^{-2} is the gravitational constant, $P \approx$ 12.42 hours is the M_2 tide period, and $H_{ave} \approx 50$ m is the Inlet's averaged water depth. This resonant scale is close to the Inlet's length; as a result, tides are significantly amplified from about ±1 m near the Gulf of Alaska opening to about ±5 m in the northern Inlet (Fig.2). The large tide produces strong currents and tidal bores with speeds ~ *4 m s^{-1}* and peak heights ~ *3 m* in the Turnagain Arm during a flood (http://tidal-bore.tripod.com/usa/_turnagain.html), and exposes extensive mud flats throughout the

upper inlet in the subsequent ebb. Wetting and drying is therefore a common and important phenomenon in the Cook Inlet. The extensive mud flats are visible from specially-processed satellite images which will be used to validate the model. In the central portion of Cook Inlet, strong oscillatory tidal currents in channels are often associated with the so-called "rip tides" (Haley et al. 2000; Okkonen and Howell, 2003); using the model calculations we will investigate possible mechanisms for this phenomenon.

In addition to tides and WAD, currents induced by buoyancy (from rivers) and winds also constitute important components of the circulation and mixing in the Cook Inlet. Fig. 3 shows the monthly discharges from seven major rivers obtained from the USGS. However, tributary discharges are significant, and the combined high discharge during spring/summer snow-melt amounts to over 5×10^3 m^3 s^{-1}, or approximately *2~3* times the combined peak discharge shown in Fig.3. The river freshening as well as tidal and wind mixing result in a partially-mixed estuary. The surface salinity S in the lower Inlet near the Stevenson-Kennedy entrance is ≈ 30~32 psu, which is a little less than the salinity values found over the adjacent shelf/slope in the Gulf of Alaska (Xiong and Royer, 1984). The Cook Inlet/Gulf of Alaska climate is extreme. Winter storms due to the Aleutian Low propagate eastward. These storms and continental drainage winds bring high wind speeds (over 20 m s^{-1}) and frigidly low air temperatures. The mean winter wind is generally westward. In summer, the Aleutian low is replaced by a weak anticyclonic system, resulting in generally eastward (and much weaker) wind (Royer, 1975).

The paper is organized as follows. Section 2 describes the Cook Inlet model setup. In section 3, we discuss tides, tidal bores and WAD processes in the upper Inlet, and compare the modeled WAD regions with remote sensing data. Section 4 examines the role of buoyancy and tides in producing 'rip tides' in the central Inlet, and section 5 concludes the paper.

2. The Cook Inlet Model Setup

The model is based on POM: three-dimensional and baroclinic with curvilinear grid in the horizontal, and terrain-following in the vertical (i.e. *sigma*-level). It incorporates a WAD algorithm that is described in great details in Oey (2005, 2006]. At each time step, a cell's face is blocked if the local water depth is less than a prescribed value (= *5 cm* is used) by setting the corresponding fluxes = *0*. However, the model solves the full set of governing equations over wet as well as dry cells, and flows across cell faces satisfy the balance equations, which dictate if the cells become wet or dry at the next time step. Dry cells are thus temporarily dormant, to be activated depending on volume and momentum (heat and salt also for general stratified flows) conservations in that cell as well as in the neighboring cells.

WAD simulations require bottom topography from deep waters to absolute land regions where the orography is sufficiently high that grid cells are *always* dry. The transition (of potential WAD region) is not well-defined for the Cook Inlet especially over the mud flats. On the other hand, NOAA/NOS' nautical charts (sounding data) do delineate potential WAD regions for boaters. We therefore interpolated the topography data set without WAD regions (which was on a *1km×1km* grid kindly provided by Dr.

Proshuntinsky, WHOI) with NOAA's potential WAD regions, so that the depth tapers to zero at the nearest absolute land points. The final depths for all water and WAD regions are then interpolated onto the model's curvilinear grid cells (Fig.3b). There are 401x151 grid points and grid sizes vary from ~1 km near the southern open boundaries of the model domain to less than 0.5 km in the north near Anchorage, and in the Knik and Turnagain Arms. Sixteen sigma levels are used in the vertical.

Comprehensive climatology that covers the entire Cook Inlet is not available, yet temperature and salinity (*T*, *S)* are required for initial and boundary conditions. Therefore, the initial *S* is set to *32.4* psu, which corresponds approximately to shelf/slope estimates off the Stevenson/Kennedy entrances (e.g., Xiong and Royer, 1984; Okkonen and Howell, 2003). With river discharges and mixing by tides, we expect that, after some time (~months), the model Inlet will establish its own salinity distribution. For temperature, GDEM climatology provides the first guess, which we modify according to NOS' measurements at Anchorage, Seldovia and Kodiak Island.

Cook Inlet's sea level contains large tidal components particularly M_2, S_2, K_1 and O_1 (Fig. 2). The largest of these, M_2, has an amplitude of about 1 m near the Stevenson and Kennedy entrances. To simplify the analysis without sacrificing essential WAD physics, most of the results shown below are from experiments that use a round-number period of 12 hours and an average amplitude η_o = 1.2 m at the model's southern open boundaries. However, we also have repeated some experiments including all tidal components. Open boundary specifications consist of a combination of normal-velocity specified as a sinusoid (amplitude $\overline{U}_{no} \approx \sqrt{g / H_{msl}}\,\eta_o$ where H_{msl} is averaged depth ≈ 70 m in the lower inlet) and radiation (Oey and Chen, 1992). The same specification is

applied to the Shelikof Strait open boundary except that when there are river discharges Q_{river}, the same outflow is allowed to exit the model domain at the strait. The zero-phase assumption between Shelikof strait and Stevenson/Kennedy entrances is an excellent one. Other open boundary specifications are as follows: one-sided advection for tangential velocities, temperature and salinity (velocities = *0* and climatological *T* and *S* during inflow), Orlanski's (1967) radiation for both components for the three-dimensional velocity, and radiation based on external gravity phase speed $\sqrt{gH_{msl}}$ on the relatively unimportant η (because normal velocity is specified).

We assume the Inlet is ice-free throughout the year, and at the surface, wind stresses are specified and heat and salt fluxes are zero. In the midst of winter (February) the "ice-free" assumption is a poor one near-shore and in the upper Inlet [Moore et al., 2000], and the model results in these regions in winter are invalid. That surface heat and salt fluxes are zero is also inaccurate especially in late fall and winter when strong evaporative losses are expected due to strong winds and low air temperatures. To partially compensate for the missing forcing, model surface temperature is relaxed to climatology with a time scale of 1.5 months. The surface salt flux is still zero, however, and the distribution of salinity inside the model Inlet is assumed to be dominated by discharge and mixing with more saline waters from the Gulf of Alaska. We use NOAA/NDBC buoy data and NOS winds at four stations: Anchorage, Nikiski, Drift River and Augustine Island; examples are shown in Fig. 4 as wind stick plots for the first 60 days of year 2000. These winds are converted to stresses using Large and Pond (1981) and linearly interpolated onto the model grid. The wind is generally weaker in the upper inlet (Anchorage) than in the lower inlet (Augustine Island); short-period fluctuations can

be seen in Fig.4 at all stations. There exist however finer spatial variability and transient wind events due to air flows over mountain ranges and through valleys (D. Prentki, 2004; private communication); these wind events are not captured well by the use of only four stations.

Discharges from seven of the larger rivers were obtained from USGS (Fig.2). As pointed out above, the values are low estimates because USGS does not include additional contributions from tributaries. Corrections provided by Dr. Prentki were used in the model. The corrected discharge totals about $5\times10^3\ m^3\ s^{-1}$ during the summer maximum. Peak discharges occur in late spring through summer, and minima are from late fall through winter. Okkonen and Howell (2003) show that salinities measured in the lower through middle Inlet reach lowest values in Fall (October~November). The lag (between peak discharge and times of freshest Inlet's waters) suggests a tide-riverine mixing time scale of about *2~3 months*. Discharge is specified as a downward vertical volume flux per unit area, w_{River} (Oey, 1996). For each river, we spread w_{River} over a (somewhat subjectively determined) area in the vicinity of that river. For the rivers in the upper Inlet, the 'spreading' is often over potential WAD cells (Fig. 3) – a situation that mimics the actual spreading of fresh waters over shallow streams.

The initial field is one of rest, velocity $\boldsymbol{U} = 0$ and *T/S* are either stratified in the vertical, area-averaged from climatology, or homogeneous depending on model experiments (below). The water level is initially at the mean sea level (MSL). Tidal velocity forcing, and/or wind and/or river are then turned on. On lateral (absolute) land boundaries, normal fluxes are nil and no-slip conditions are applied. Bottom friction is computed either by using a bottom drag coefficient C_z obtained by matching the near-

bottom modeled velocity to the Law of the Wall, or simply a constant C_z (see Mellor, 2004, and the WAD implementation in Oey, 2006). Smagorinsky's (1963) shear and grid-dependent formula for horizontal viscosity and diffusivity are used with their ratio = *5* and the Smagorinsky's constant = *0.1*.

We have carried out various experiments to systematically test the model (Table 1). Experiments 2Dpom and 2Dwad are two-dimensional barotropic experiments forced only by tides at the open boundaries, but with the WAD scheme turned off (2Dpom) and on (2Dwad), respectively. For these 2D calculations, quadratic bottom friction formula using the depth-averaged velocities is used, with C_z a constant = *0.0025*. Experiment 3Dtidehom is the full three-dimensional POM-WAD but the water is homogeneous. The integration is for *120 days*. Experiment 3Dtide is the full three-dimensional (baroclinic) POM-WAD in which stratification exists because of initial, surface and open-boundary *T/S* climatology, but river discharge is nil. Experiment 3Driv turns on river runoffs. River forcing is intentionally extreme (to test POM-WAD): corrected peak discharges (late spring through summer) from the seven rivers (Fig. 3) are specified, and they are held steady for two years. The total is $5\times10^3\ m^3\ s^{-1}$. Year 1 is without wind, but with tide, so that the model establishes a quasi-equilibrium state (in salinity distribution in particular). In year 2, six-hourly winds that correspond to the year 2000 (linearly interpolated as described above) are also used. Finally, Experiment 3Drivsea uses seasonal river inputs instead of keeping them steady. Experiments 3Driv and 3Drivsea were conducted with both the single-component and all-component tidal forcing along the open boundaries, described previously.

3. Tides and WAD Processes in the Upper Cook Inlet

3.1 Model simulations of tides and salinity

We focus on Experiment 3Driv, and discuss other cases when appropriate to draw contrasts. Since tidal resonance is an essential feature of the Cook Inlet's WAD and circulation dynamics, we first show in Fig.5 an example of the phenomenon with plots of 5-day modeled and observed sea-levels at the lower (Kodiak), central (Nikiski) and upper inlets (Anchorage). The simulated sea-level compares well with that observed, both in terms of the phasing and the amplification of sea-level from Kodiak to Anchorage. In addition to inadequate model physics, discrepancies are in part due to inexact knowledge of the open-boundary conditions, which may be refined as described in Chen and Mellor [1999]; but this has not been done here.

Fig. 6 shows salinity distributions at four tidal stages in the upper Inlet. At the beginning of flood (Fig. 6a), extensive "dry" areas (they are really "mud flats") can be seen south and southeast of Anchorage in the wide entrance to Turnagain Arm. "Dry" areas are also seen in the northern portion of the Upper Inlet especially in the upper Knik Arm. Three hours later (Fig. 6b), more saline flood waters begin to fill the upper inlet. The peak flood currents are strong, up to 3~4 m s^{-1} at some location. The flooding is complete in Fig. 6c, in which one sees the filling-up of flood waters in the upper inlet (all model grid cells are "wet" at this stage). Saline waters can clearly be seen to intrude into the two Arms. Three hours later (Fig. 6d), strong ebbing currents ensue with peak speeds of 5~6 m s^{-1}. The strong speeds (at peak flood in particular) occur in local regions where the water layer is thin (< 0.5 m) and often produce supercritical flows

accompanied by hydraulic jumps during the flood ("tidal bores," see below). Note that in addition to tides, Fig. 6 also shows the wind vectors (in red). However, winds are generally weak in the upper inlet near Anchorage (Fig. 4), and we find that wind effects are usually overwhelmed by the strong tides.

3.2 Remote sensing data

The extensive "dry" regions in the Turnagain Arm south-southeast of Anchorage (seen in Fig. 6a) are well-known to local residents, and can be seen from the highway along the northern bank (Fig. 7). However, there are no direct measurements of the extent and variability of the mud flats. To lend support to the modeled WAD regions, we examine remote sensing data. High-resolution remote sensing data, such as those from Landsat TM or ETM+ (30-m resolution), are sporadic (16-day revisit time) with limited coverage (100–200 km) and high cost, not to mention the frequent cloud cover. Traditional operational satellite ocean color sensors such as the Coastal Zone Color Scanner (CZCS, 1978-1986) and the Sea-viewing Wide Field-of-view Sensor (SeaWiFS, 1997 – present) provide coarse resolution data at about 1-km/pixel. This is insufficient for the purpose of delineating small scale WAD features. On the other hand, the MODerate resolution Imaging Spectroradiometer (MODIS) instruments aboard the Terra (morning pass, 1999 – present) and Aqua (afternoon pass, 2002 – present) satellites are equipped with several medium-resolution bands at about 250-m/pixel or 500-m/pixel. These medium-resolution data have shown unprecedented capability for coastal studies, for example in the detection of oil spills (Hu et al. 2003) and assessment of coastal/estuarine water quality (Hu et al. 2004; Miller and McKee 2004). These data are

therefore preferred in the present study not only because of their resolution, but also because of the repeated coverage that is available at high latitudes due to the polar orbit of the Terra and Aqua satellites, which allows multiple views of the Cook Inlet region within repeated tidal cycles. At the latitude of Cook Inlet, MODIS instruments provide 2-4 images per day between 21:00 and 23:50GMT under ambient sunlight and during some phases of the tidal cycle. Water absorbs most of the light in the red and near infrared, and is completely opaque in the mid infrared. This makes it easy to delineate water from any other non-water surface. The absorption coefficient (a_w) of water in the blue-green wavelengths is less than 0.1 m^{-1}, but is significantly larger in the longer wavelengths. For example, at 645-nm and 859-nm (the MODIS 250-m bands), a_w = 0.325 m^{-1} and 4.19 m^{-1}, respectively. Because remote sensing reflectance, R, is inversely proportional to a_w, R(859-nm) is very small (<0.001 sr^{-1}) unless there is significant amount of suspended sediments (e.g., > 100 mg L^{-1}) in the water or the bottom is shallow (< 2 m) but bright. Therefore, the 859-nm and 645-nm MODIS bands can be used to detect water/land interface as well as submerged land surface.

For the purpose of delineating WAD regions and (qualitatively) comparing them with the model simulation (Fig.6), we take advantage of the periodicity of the process so that only the stage of tide is relevant rather than the actual date and time. In the followings, we therefore choose the clearest images that are available at the appropriate tidal stages as determined from the NOS sea-level charts, and compare the images with the model. Fig. 8 shows the "true color" MODIS images corresponding to approximately one-hour before a low water level at Anchorage (23:15 GMT on July 22, 2005; Fig. 8a), and one-hour before a high water level (21:05 GMT on August 27, 2005;

Fig. 8b). We focus on the Upper Inlet portion of the MODIS images in a domain slightly larger toward the west than that shown in Fig. 6. During low tide (Fig. 8a, which can be compared with Fig.6a) the mud flats regions on both the northern and southern banks of Turnagain Arm (south/southeast of Anchorage) are clearly seen as darker shades of gray relative to lighter shades representing sediment-rich water. Other mud flats regions can also be seen in Fig.8a: in the upper Knik Arm northeast of Anchorage, and in the form of an arc outside a river mouth along the northern coast of the Upper Cook Inlet (upper center of the image). Despite the uncertainty in the detailed model topography over the mud flat areas, the satellite images are in good agreements with the predicted "dry" regions of Fig. 6a. MODIS images are useful also in delineating details of the mud flats morphology at different times. Fig. 9 shows an enlarged image of the mud flats region south/southeast of Anchorage at two different times: 23:15 GMT on July 22, 2005 (lower panel; same time as in Fig. 8a) and 1 hour and 45 minutes earlier at 21:30 GMT (upper panel). While the former shows almost-completely exposed mud flats (dark shades), the latter shows intertwined light and dark shades indicative of a more complex morphology due to unevenly submerged mud flats (the ellipses in Fig. 9 highlight the regions with significant changes; the larger ellipse is ~ 15 km across).

During high tide (Fig. 8b, which can be compared with Fig. 6c) most of the mud flats mentioned before are submerged and covered by murky turbid waters (brownish color) and more saline waters (clear and bluish colors) that have now penetrated from the lower Inlet. The saline intrusion is particularly pronounced along the deep channel south of the Forelands (east of Kalgin Island, lower-left corner of Fig. 8b) and will have

important dynamical implications, to be discussed later in conjunction with the model results.

3.3 WAD effects on tidal amplitudes and phases

WAD processes alter the surface area and total volume of an estuary so that tidal amplitude and phases change when compared to the case without WAD. Fig. 9 compares (harmonically analyzed) M2 tidal amplitudes and phases for the two cases (2Dpom and 2Dwad) focusing on the Upper Inlet only. (In the Lower Inlet, south of the Forelands, there are only slight differences between the two cases.) The comparisons are made only for those grid cells that are always wet. Large differences can be seen: amplitudes for 2Dwad are approximately *20%* larger and the corresponding phases lag 2Dpom by about *10%*. The slower phase for 2Dwad may be explained by the water-retention property of the WAD physics that creates tidal asymmetry between flood and ebb (c.f. Oey, 2005). Since tidal energy fluxes into the Upper Inlet through the Forelands are approximately equal for the two cases, the larger amplitudes for 2Dwad are due to its effectively smaller storage volume in the Upper Inlet due to the presence of WAD areas.

3.4 Tidal bores in the Turnagain Arm

In the Science Forum website of the University of Alaska Fairbanks [http://www.gi.alaska.edu/ScienceForum/water.html], Larry Gedney observed: "Driving the Seward Highway along Turnagain Arm … one may occasionally observe a white, frothy line of turbulent water extending completely across the arm and moving slowly

upstream… This is a tidal bore. It is created when rising tides in Cook Inlet encounter the constricted entrance and diminishing water depths of Turnagain Arm…" Because of large tidal ranges, currents in the Upper Inlet are very strong. During a flood, the tail portion of the rising tide propagates faster than its front, the forward characteristics intersect producing a hydraulic jump that constitutes the model "bore." To examine this phenomenon we plot vertical section contours of velocities along the Turnagain Arm (section B in Fig. 11). Fig. 12 shows the along-section velocity in Turnagain Arm every hour, beginning with one hour after flood begins (labeled "Hour=04"). In the next six hours (panels) one can see a bore-like structure in which the sea surface develops a 'dip' of about *2 m*, propagating up the Turnagain Arm at about *3~4 m* s^{-1} (*10~15 km per hour*). These values are consistent with those given previously in the Introduction. The tourist information (for those waiting to view the bore along the Arm), for example, indicates that the bore arrives at Bird Point (the middle of the shallow Arm, X ≈ *60~70 km* in Fig. 12) about one hours after it is seen entering the shallow Arm in Beluga Point (X ≈ *50 km*). The simulations also show detailed variations in the flow velocity and wave propagation speed along the Arm. In the Turnagain Arm, for example, flood starts in the deeper part (Hour=4) when the shallow region is still draining (blue colors), which produces a salinity front near x ≈ 45 km (see Fig. 13 below).

3.5 Tidal advection and mixing of salinity in Upper Cook Inlet

Fig. 13 contrasts the salinity at the three sections (A, B and C in Fig. 11) during low (left column) and high tides. The dry areas at low tide are clearly seen for section A. Those at sections B and C cannot be seen, since rivers are specified and grid cells are

always wet along the center-axes of the Turnagain and Knik Arms. One sees however pockets of water left in local topographic 'bowls' in these Arms at low tides. In general, water along the Knik Arm is less saline and the salinity front propagates farther into the deeper inlet than in the Turnagain Arm. There are two reasons for that asymmetry between the two Arms. First, the river inputs from the Knik Arm are larger than the river inputs into the Turnagain Arm, and second, the topography along the Knik Arm is steeper compared with the flat end of the Turnagain Arm, allowing faster flushing out of waters from the Knik Arm during an ebb. Note also the strong vertical mixing produced by the tides and strong gradients across the entrance to the Knik Arm (upper right panel of Fig. 13). A similar phenomenon of strong cross-channel density gradients also occur in the central Inlet which we now discuss.

4. Processes in the central Cook Inlet and "rip tides"

Fig. 11 shows the three sections in the vicinity of Kalgin Island where strong tidal currents have been observed. Drifters launched in the central inlet show strong tidally-driven oscillatory flow whereas the drifters are often "trapped" over the deep channel, moving back and forth for days (Dr. Mark Johnson, 2005, *personal comm.*. www.ims.uaf.edu/research/johnson/cmi). The strong currents are often referred to as "rip tides" (Haley et al. 2000; Okkonen and Howell, 2003), and they have scales of a few hundred meters. In the model, these features are diffused but are still discernible. We now show that these "rip tides" are due to strong fronts caused by confluences of saline (i.e. ocean) and less-saline (i.e. rivers) water masses. Stratification (horizontal and vertical) is essential for their existence. Fig. 14 shows contours of stream function

superimposed on color images of salinity at the Kalgin Island section (marked "I=180" for the model grid line number) and another section some 40 km to the south ("I=140"). These contours correspond to one hour before the peak (high) tide and one can see the intrusion of high-salinity water due to the flooding currents on the left side of the "I=140" section, as well as in the deep channel on the left side of the Kalgin Island section (the "I=180" section). Such salinity intrusion during flood was previously noted in MODIS image in Fig.8b. Fig. 14 shows re-circulating cells at both sections but particularly at the section off the Kalgin Island (I=180); the convergent region between the two opposite-signed re-circulating cells defines the front at this stage of the tidal cycle. The salinity difference across the front is 1-1.5 psu. Fig. 15 gives more details of the flow field at the Kalgin Island section. The figure shows strong flood (U – the through-section or along-channel component from southwest to northeast up the Inlet, Fig. 15a) with velocity $U \approx 2$ m s^{-1} at the frontal zone and clear convergence shown by the cross-channel velocity (V, Fig. 15c). Upwelling and downwelling velocities (Fig. 15b) of $W \approx \pm 25$ m day^{-1} create cross-channel circulation cells seen by the stream function (Fig. 15d).

To test the importance of rivers and associated stratification in the dynamics of these circulation cells, Fig. 16 compares the results of the realistic model case with seasonal river input (3Drivsea) against the experiment in which river runoffs are null (3Dtide) and also against the experiment without stratification (3Dtidehom). Note that only the wider channel south of the Kalgin Island (the left part of Fig. 15b) is shown. The front over the deepest part of the channel is formed only in the case when there is river discharge (Fig. 16a) and also at times of flood when large amount of saline water intrudes into the Inlet through the deep channel (Fig. 17). The model results here are

qualitatively similar to the observations of Okkonen and Howel (2003) taken across Kalifornsky Beach (Fig. 11), although a more detailed comparison is not warranted due to the idealized nature of the model forcing we have used. Haley et al. (2000) also note that "rip tides" occur most often during flood, with strong current speeds of about 2-3 m s^{-1} east of Kalgin Island. It is quite possible that the higher observed speeds may be at times caused by the wind forcing, but the combined mechanism of tidal current and buoyancy, proposed above, is robust; i.e. the phenomenon repeats for each tidal cycle.

5. Discussion and Conclusions

A wetting and drying algorithm for POM in its most general three-dimensional settings with stratification and forcing is implemented and applied to study the WAD and circulation processes in the Cook Inlet, Alaska. The model incorporates high-resolution and realistic topography with WAD regions. The model includes tidal forcing, river discharge, temperature and salinity fields along the open boundaries, and wind forcing. Cook Inlet is an environmentally sensitive region with harsh conditions; it is an excellent place to test a model with WAD under extreme forcing that includes large tidal ranges and strong currents. Over a tidal cycle, the model simulates complex WAD regions that compare quite well with MODIS satellite images, despite the uncertainty of the detailed mud flat regions. In this regard, we have demonstrated the usefulness of the fine-resolution MODIS images in detecting "dry" and "wet" regions, hence also in evaluating the WAD processes. In the future, one may use multiple images to map the mud flat areas at different stages of the tidal cycle (with more extensive temporal and spatial coverage than that shown here in figures 8 and 9, and with the possible usage of the near-

IR and mid-IR bands) to improve the representation of the mud flats topography in the model. The same methodology may lead to improved flood predictions in other circumstances (e.g., tsunamis, storm surges, etc.). In the upper Inlet, the model simulates wetting and drying processes that affect tidal amplitudes and phases. The model simulates the propagation of bore-like features over the shallow mud flats of the Turnagain Arm, with height and propagation speeds in rough agreements with the experiences of local observers (there are no direct measurements over the mud flats). In the central Inlet, the model shows upwelling and downwelling cells with strong horizontal and vertical velocities. These strong currents are caused by fronts produced by convergence of saline water from the lower inlet through the deep channel with fresher water of the upper Inlet. River inputs coupled with tides are essential to the existence of these fronts, as shown by sensitivity experiments with and without rivers. This study describes complex dynamics of an inlet with extreme tides using a model that includes the WAD algorithm. Future research may include further model evaluations and developments of new model components such as sediment transports associated with WAD, and also wave-current interactions (Mellor, 2003).

Acknowledgements The study was supported by the Mineral Management Service (Contract #1435-01-03-CT-72021); Oey and Ezer were also partly supported by ONR grants; Hu and Muller-Karger were supported by NASA grants. NOAA/GFDL provided computational resources.

References

Balzano, A., 1998: Evaluation of methods for numerical simulation of wetting and drying in shallow water flow models. *Coastal Engineering*, 34, 83-107.

Beaglehole, J.C., 1974: "The Life of Captain James Cook." Stanford Univ. Pr. Stanford-CA. 760pp.

Blumberg, A. F. and G. L. Mellor, 1987: A description of a three-dimensional coastal ocean circulation model. *Three-Dimensional Coastal ocean Models*, N. Heaps, Ed., American Geophysical Union, 208 pp.

Casulli, V. and R. Cheng, 1992: Semi-implicit finite difference methods for three-dimensional shallow water flow. *International Journal for Numerical Methods in Fluids,* 15, 629-648.

Chassignet, E.P., L.T. Smith, G.R. Halliwell, and R. Bleck, 2003: North Atlantic simulations with the hybrid coordinate ocean model (HYCOM): impact of the vertical coordinate choice, reference pressure and thermobaricity, *J. Phys. Oceanogr.*, 33, 2504-2526.

Chen, C., R. C. Beardsley and G. Cowles, 2006: An unstructured grid, finite-volume coastal ocean model (FVCOM) system. Oceanography, 19(1), 78-89.

Chen, P. and G.L. Mellor, 1999: Determination of tidal boundary forcing using tide station data. Coastal Ocean Prediction, Coastal and Estuarine Studies, Vol. 56, C. N. K. Mooers (Ed.), American Geophysical Union, Washington, DC, 329-351, 1999.

Cheng, R.T., V. Casulli and J.W. Gartner, 1993: Tidal, residual, intertidal mudflat (TRIM) model and its application to San Francisco Bay, California. *Estuarine, Coastal & Shelf Sci.,* 36: 235-280.

Drillet, Y., Bourdallé-Badie, R., Siefridt, L., Le Provost, C., 2005: Meddies in the Mercator North Atlantic and Mediterranean Sea eddy-resolving model. *Journal of Geophysical Research*, VOL. 110, C03016, doi:10.1029/2003JC002170.

Ezer, T. and Mellor, G.L., 2000. Sensitivity studies with the North Atlantic sigma coordinate Princeton Ocean Model. Dyn. Atmos. Ocean, 32, 185-208.

Fan, S.J., L.-Y. Oey, and P. Hamilton, 2004. Assimilation of drifters and satellite data in a circulation model of the northeastern Gulf of Mexico. Cont. Shelf Res., 24(9): 1001-1013.

Flather, R.A. and K.P. Hubbert, 1990: Tide and surge models for shallow-water-Morecambe Bay revisited. *Modeling Marine Systems,* Vol. I, Editor: A.M. Davies, CRC Press, 135-166.

Gill, A.E., 1982: "Atmosphere-Ocean Dynamics." Academic Press, New York, 662pp.

Haley, B., G. Tomlins, O. Smith, W. Wilson and M. Link, 2000: Mapping Cook Inlet rip tides using local knowledge and remote sensing. MMS Report, OCS Study, MMS 2000-025.

Hu, C., F. E. Muller-Karger, C. Taylor, D. Myhre, B. Murch, A. L. Odriozola, and G. Godoy, 2003: MODIS detects oil spills in Lake Maracaibo, Venezuela. Eos. AGU Trans. 84(33):313,319.

Hu, C., Z. Chen, T. D. Clayton, P. Swarzenski, J. C. Brock, and F. E. Muller-Karger, 2004: Assessment of estuarine water-quality indicators using MODIS medium-

resolution bands: Initial results from Tampa Bay, Florida. Remote Sens. Environ. 93:423-441.

Ji, Z.G., M.R. Morton, and J.M. Hamrick, 2001: Wetting and drying simulation of estuarine processes. *Estuarine, Coastal & Shelf Sci*., 53, 683-700.

Ko, Dong S., Ruth H. Preller, and Paul J. Martin, 2003: An Experimental Real-Time Intra Americas Sea Ocean Nowcast/Forecast System for Coastal Prediction, Proceedings, AMS 5th Conference on Coastal Atmospheric & Oceanic Prediction & Processes.

Kou, L. D. Labrie and P. Chylek, 1993: Refractive indices of water and ice in the 0.65-2.5μm spectral range," Appl. Opt., 32, 3531--3540.

Large, W. G. and S. Pond, 1981: Open ocean momentum flux measurements in moderate to strong winds. J. Phys. Oceanogr., 11, 324-336.

Lin, B. and R.A. Falconer, 1997: Three-dimensional layer-integrated modeling of estuarine flows with flooding and drying, *Estuarine, Coastal & Shelf Sci.,* 44, 737-751.

Lynch, D.R. and W.G. Gray, 1980: Finite-element simulation of flow in deforming regions. *J. Comp. Phys.*, 36, 135-153.

Marchesiello, P., J.C. McWilliams, and A. Shchepetkin, 2003: Equilibrium structure and dynamics of the California Current System, J. Phys. Ocean. 33, 753-783.

Mellor, G. L.. 2003: The three-dimensional current and surface wave equations. J. Phys. Oceanogr., 33, 1978-1989.

Mellor, G.L., 2004: Users' guide for a three-dimensional, primitive equation, numerical ocean model. Program in Atmospheric and Oceanic Sciences, Princeton University, 42pp. (http://www.aos.princeton.edu/WWWPUBLIC/htdocs.pom).

Mellor, G. L. and T. Yamada, 1982: Development of a turbulent closure model for geophysical fluid problems. *Rev. Geophys. and Space. Phys.*, **20,** 851-875.

Miller, R.L. & Mckee, B.A., 2004: Using MODIS Terra 250 m imagery to map concentrations of total suspended matter in coastal waters. Remote Sensing of Environment, 93, 259-266.

Moore, S. E., K. E. W. Shelden, L. K. Litzky, B. A. Mahoney, and D. J. Rugh, 2000: Beluga, *Delphinapterus leucas*, habitat associations in Cook Inlet, Alaska. Mar. Fish. Rev. 62(3): 60–80

Oey, L.-Y., 1996: Simulation of mesoscale variability in the Gulf of Mexico. J. Phys. Oceanogr. 26, 145-175.

Oey, L.-Y. 2005: A wetting and drying scheme for POM. Ocean Modelling, 9, 133-150.

Oey, L.-Y. 2006: An OGCM with movable land-sea boundaries. Ocean Modelling, 13(2), 176-195.

Oey, L.-Y. and P. Chen, 1992: A model simulation of circulation in the north-east Atlantic shelves and seas, *J. Geophy. Res.,* 97, 20,087-20,115, 1992.

Oey, L.-Y., H.-C. Lee and W. J. Schmitz Jr., 2003: Effects of Winds and Caribbean Eddies on the Frequency of Loop Current Eddy Shedding: A Numerical Model Study, J. Geophys. Res., 108 (C10), 3324, doi:10.1029/2002JC001698, 2003.

Oey, L.-Y., T. Ezer, G. Forristall, C. Cooper, S. DiMarco and S. Fan, 2005: An exercise in forecasting loop current and eddy frontal positions in the Gulf of Mexico. Geophys. Res. Let., 32, L12611, 10.1029/2005GL023253.

Okkonen, S. R. and S. S. Howell, 2003: Measurements of temperature, salinity and circulation in Cook Inlet, Alaska. Report, OCE Study MMS 2003-036, Mineral Management Service, 28 pp.

Romanou, A., E. P. Chassignet, and W. Sturges, 2004. The Gulf of Mexico circulation within a high resolution numerical simulation of the North Atlantic Ocean.. J. Geophys. Res., 109, CO1003, doi: 10.1029/2003CJ001770.

Royer, T.C., 1975: Seasonal variations of waters in the northern Gulf of Alaska. *Deep Sea Res.*, 22, 403-416.

Sheng, J. and L. Tang, 2003. A Numerical study of circulation in the western Caribbean Sea. J. Phys. Oceanogr., 33, 2049-2069.

Smagorinsky, J., 1963: General circulation experiments with the primitive equations. Part I: the basic experiment. *Mon. Wea. Rev.,* 91, 99-164.

Smith, R.D., M.E. Maltrud, F.O. Bryan and M.W. Hecht, 2000. Numerical simulation of the North Atlantic Ocean at 1/10 deg. J. Phys. Oceanogr., 30, 1532-1561.

Stelling, G.S., A.K. Wiersma and J.B.T.M. Willemse, 1986: Practical aspects of accurate tidal computations. *J. ASCE Hydraulic Engineering*, 9, 802-817.

Titov, V.V. and C.E. Synolakis, 1997: Extreme inundation flows during the Hokkaido-Nansei-Oki tsunami. *J. Geophys. Lett.,* 24, 1315-1318.

Xie, L., L. J. Pietrafesa, and M. Peng, 2003: Incorporation of a mass-conserving inundation scheme into a three-dimensional storm surge model. J. Coastal Res., 1-17.

Xiong, Q. and T.C. Royer. 1984. Coastal temperature and salinity in the northern Gulf of Alaska, J. Geop. Res., 89:8061-8066.

Table 1. Model experiments.

Experiment	**Stratification**	**Wind**	**River**	C_z	**Integration Period**	**WAD**
2Dpom	No	No	No	*0.0025*	*30 days*	No
2Dwad	No	No	No	*0.0025*	*30 days*	Yes
3Dtidehom	No	Yes	No	variable*	*120 days*	Yes
3Dtide	*Climatology*	Yes	No	variable*	*120 days*	Yes
3Driv*	*Climatology*	Yes	Yes - high	variable*	*1 Year* + *Yr.2000*	Yes
3Drivsea*	*Climatology*	Yes	Seasonal	variable*	*1 Year* + *Yr.2000*	Yes

* see Mellor (2004) and Oey (2006)

+ *1 Year* without wind, then continued with *Yr.2000* wind.

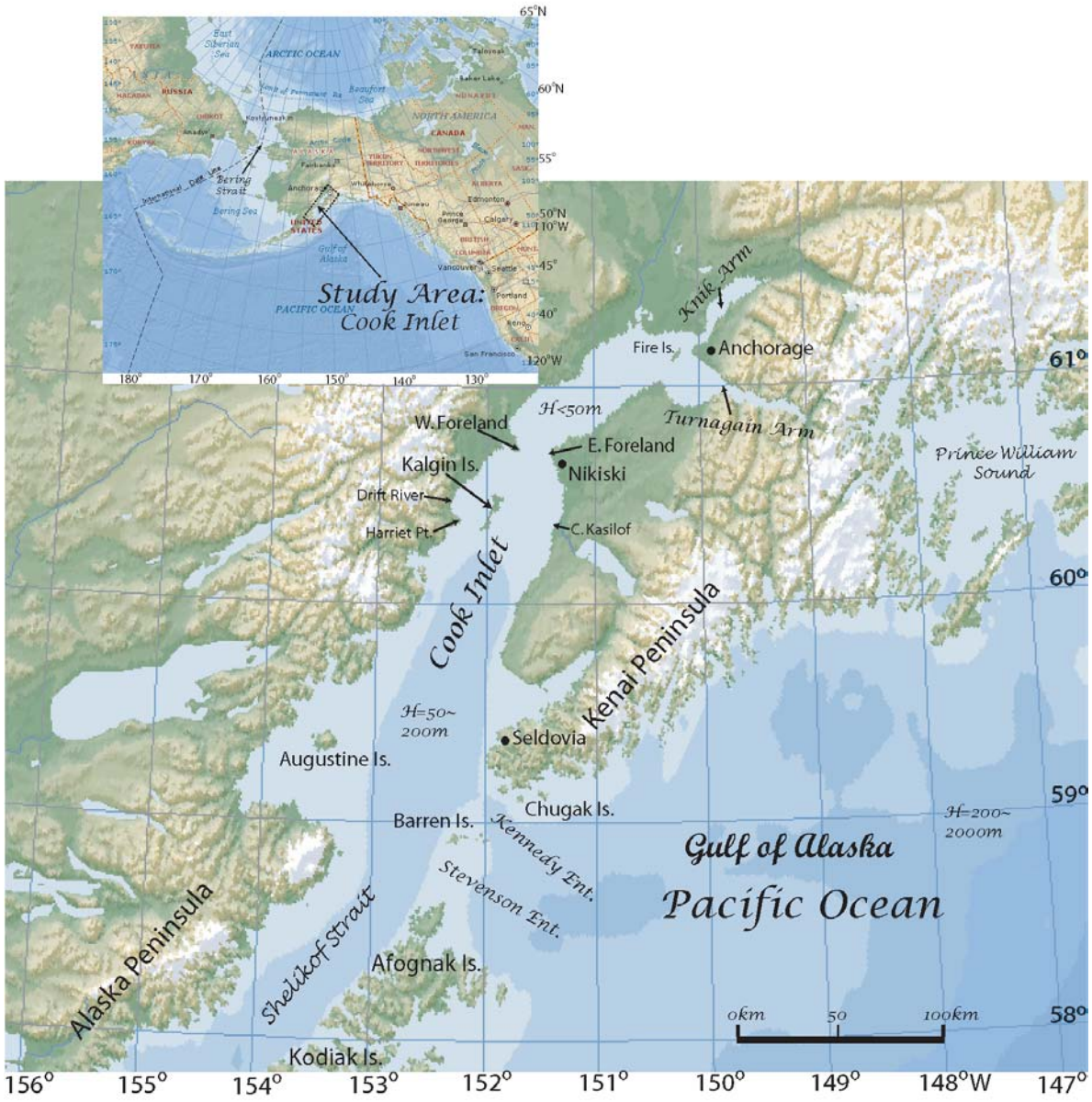

Fig. 1. Map of the Cook Inlet region in the northeastern Pacific (small inset) and the major (crude) topographic and geographic features.

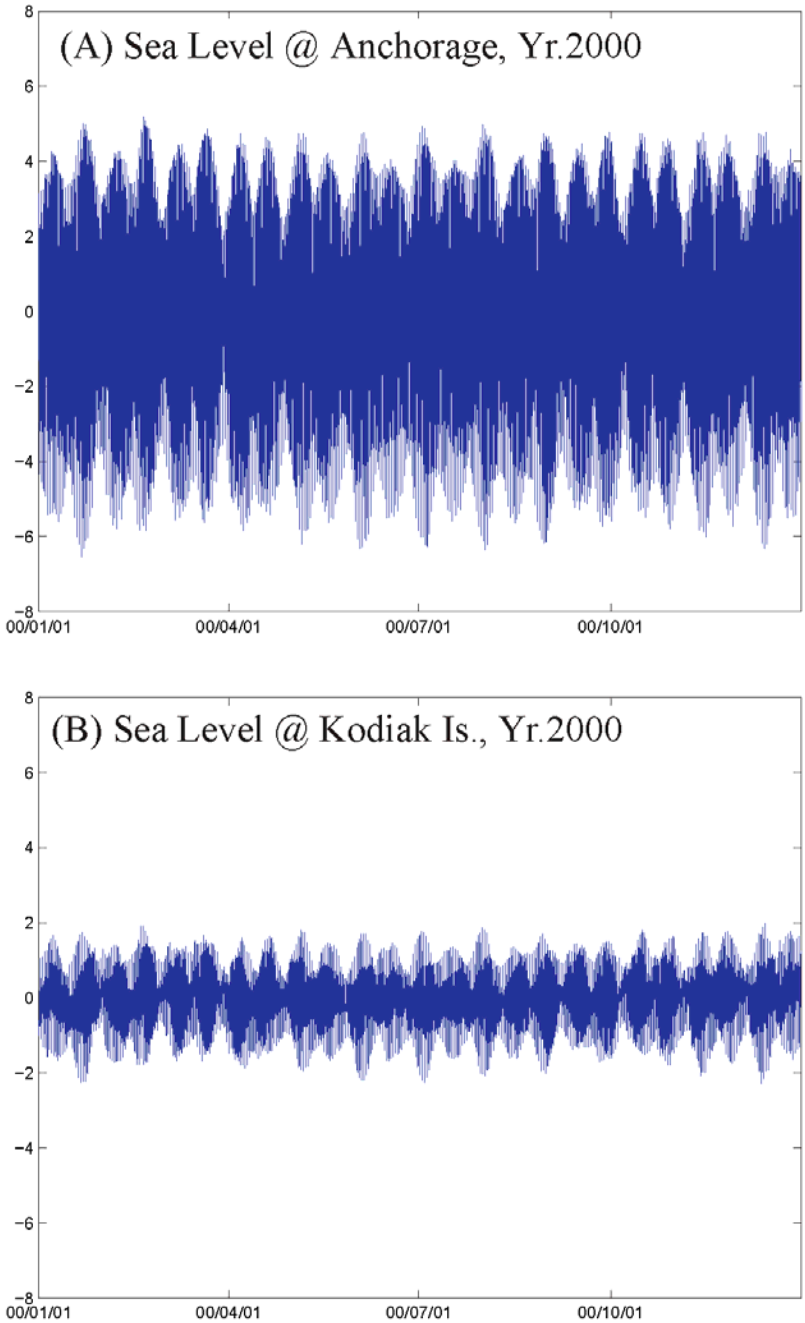

Fig. 2. Observed hourly sea level (in meters) at (a) Anchorage and (b) Kodiak Island during 2000.

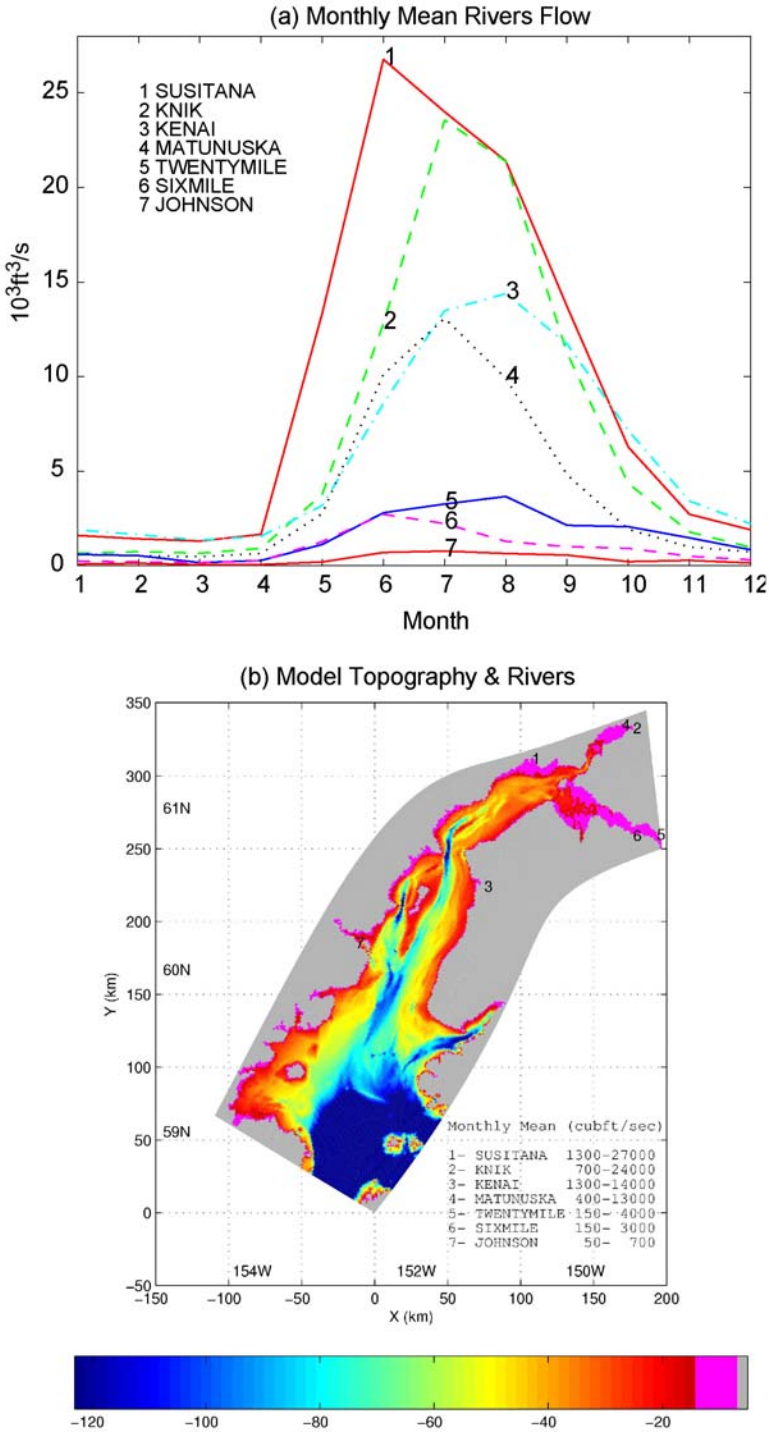

Fig. 3. (a). USGS monthly mean river discharges (plotted in the original unit in ft^3s^{-1}; 1 $m^3s^{-1} \approx 27$ ft^3s^{-1}) from seven major rivers into the Cook Inlet. (b). Location of the seven rivers marked on the model topography (in meters below a land datum; see Oey, 2006). Gray color represents the absolute land region that is always dry, magenta color represents the WAD region that can be wet or dry.

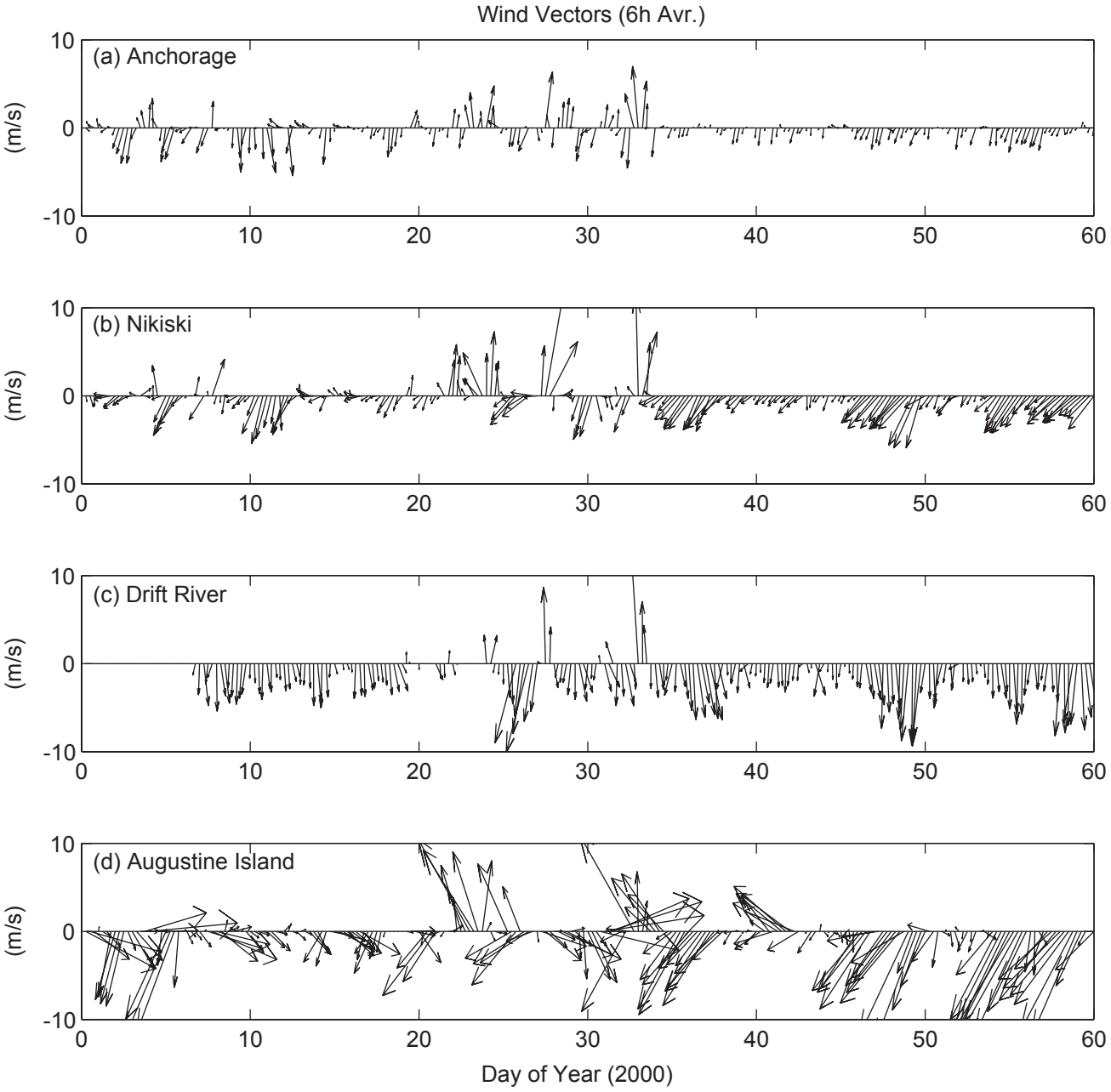

Fig. 4. The observed wind vector stick plot at four stations for the first 60 days of the year *2000*; 6-hourly averages were calculated from the NOAA meteorological stations.

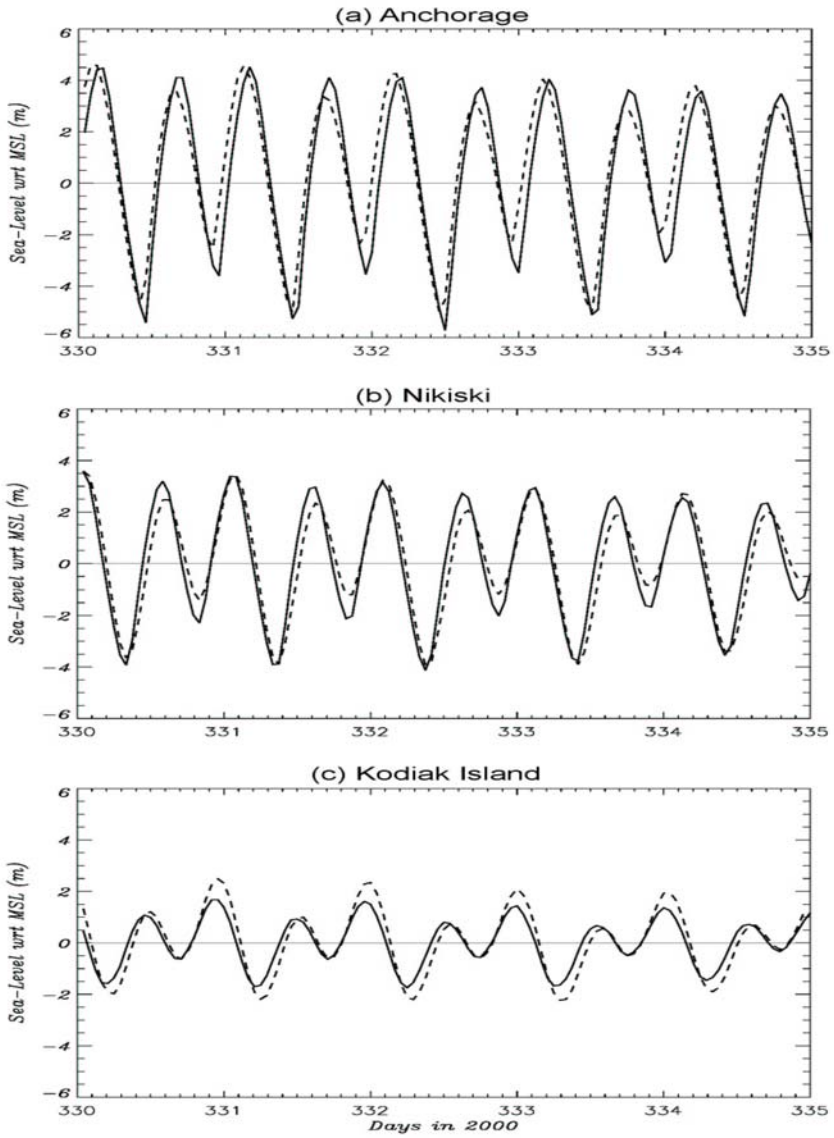

Fig. 5. Example of 5 days (in 2000) sea level variations at (from north to south) (a) Anchorage, (b) Nikiski and (c) Kodiak Island. Solid lines are observations and dash lines are from model simulations using observed tidal forcing at the open boundaries.

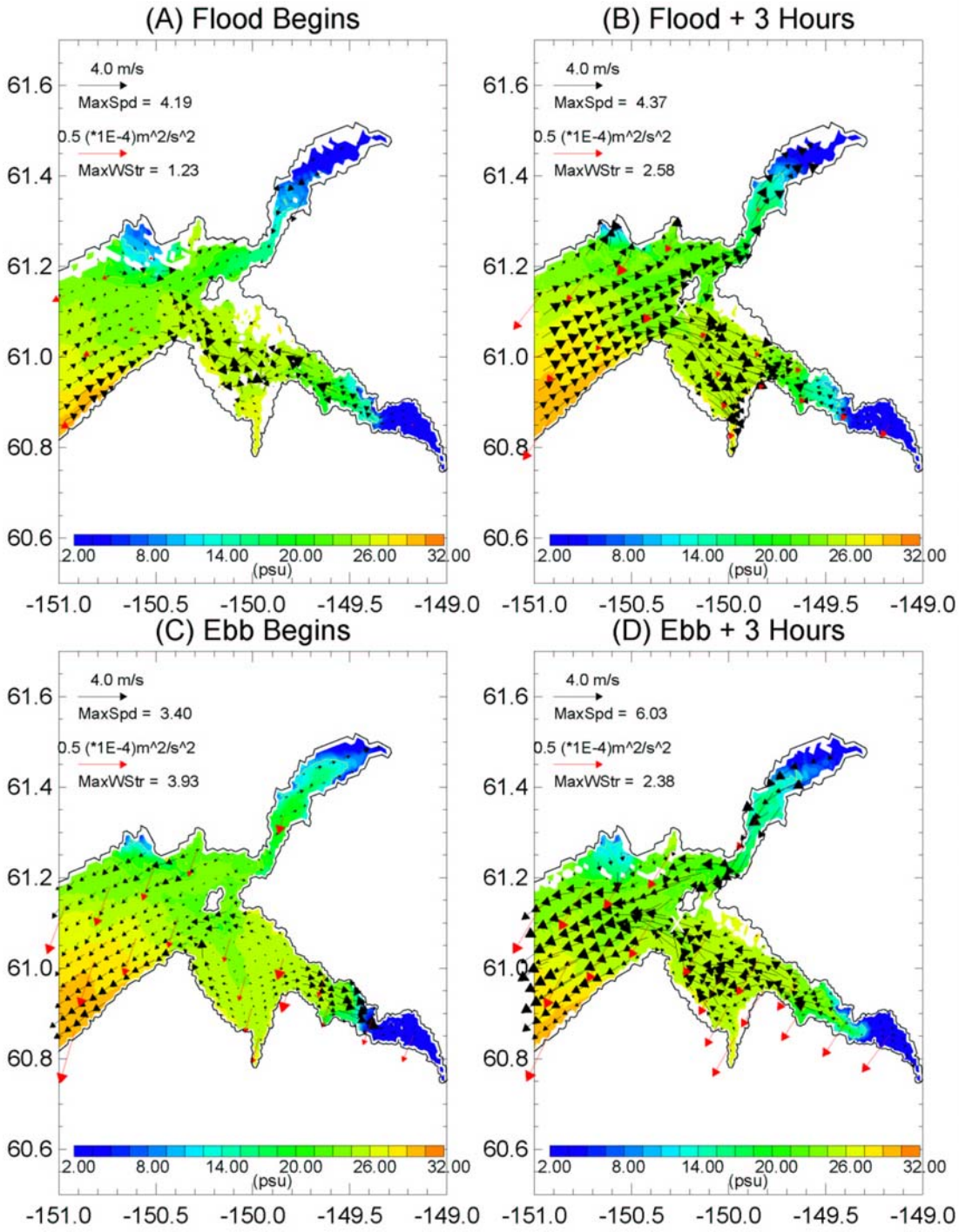

Fig. 6. Simulation of tides and river run-off in Cook Inlet, Exp. 3Driv. Shown here is an enlarged region of the upper inlet. Velocity vectors (black) at the first σ-grid nearest the surface are shown superimposed on color images of the corresponding salinity at four different phases of a tidal cycle. Red vectors indicate wind stresses used in the model at the indicated dates. Black contour indicates coastline and white regions show dry (and land) areas.

Fig. 7. A photo of dry regions consisting of frozen mud in the lower Turnagain Arm south-southeast of Anchorage just before flood in the Upper Cook Inlet (i.e. low tide, corresponding to approximately the tidal stage shown in Fig.6A). The view is towards the southwest across the Inlet. (This photo was taken in early March of 2005 by LYO).

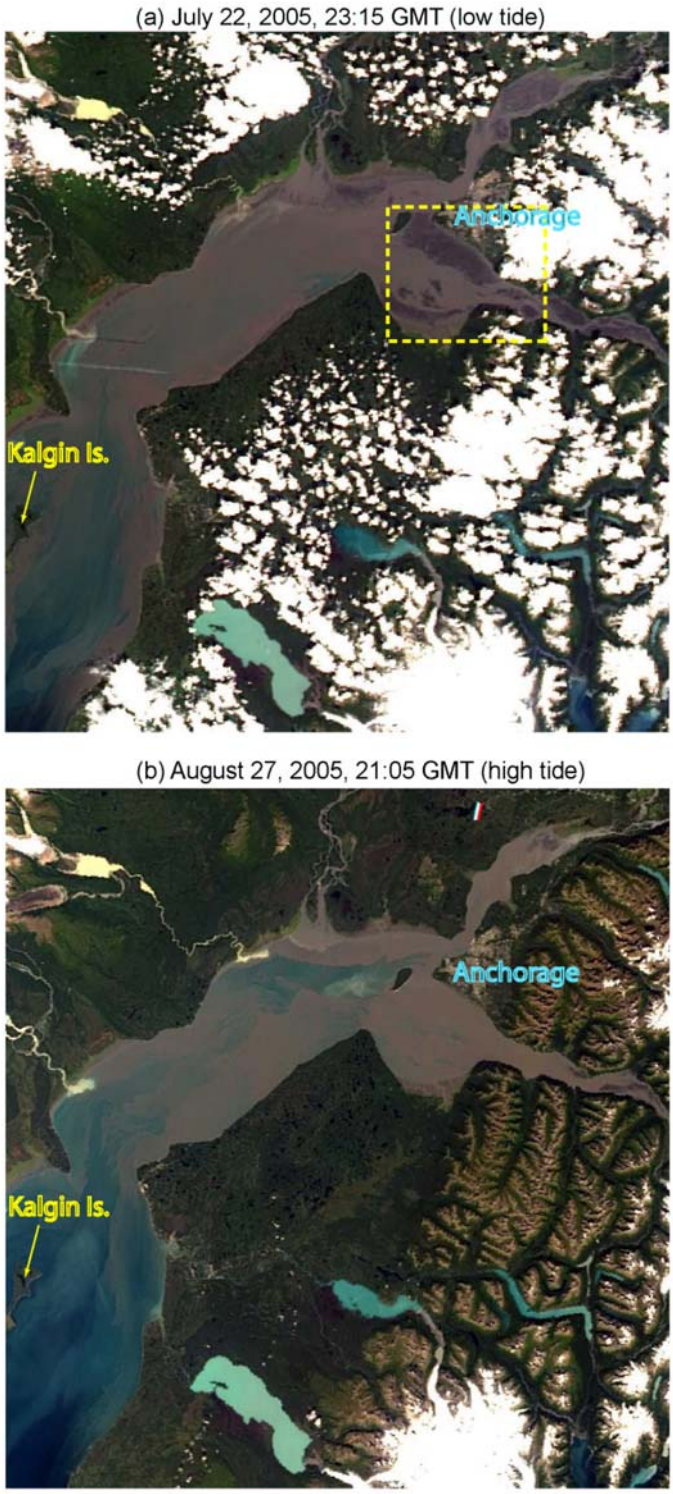

Fig. 8. MODIS/Aqua (a) and MODIS/Terra (b) true-color (RGB) images in Upper Cook Inlet: (a) near low tide (23:15 GMT) at Anchorage on July 22, 2005, and (b) near high tide (21:05 GMT) on August 27, 2005. The RGB images were composed using the three MODIS bands at 645-nm (R, 250-m), 555-nm (G, 500-m), and 443-nm (B, 500-m).

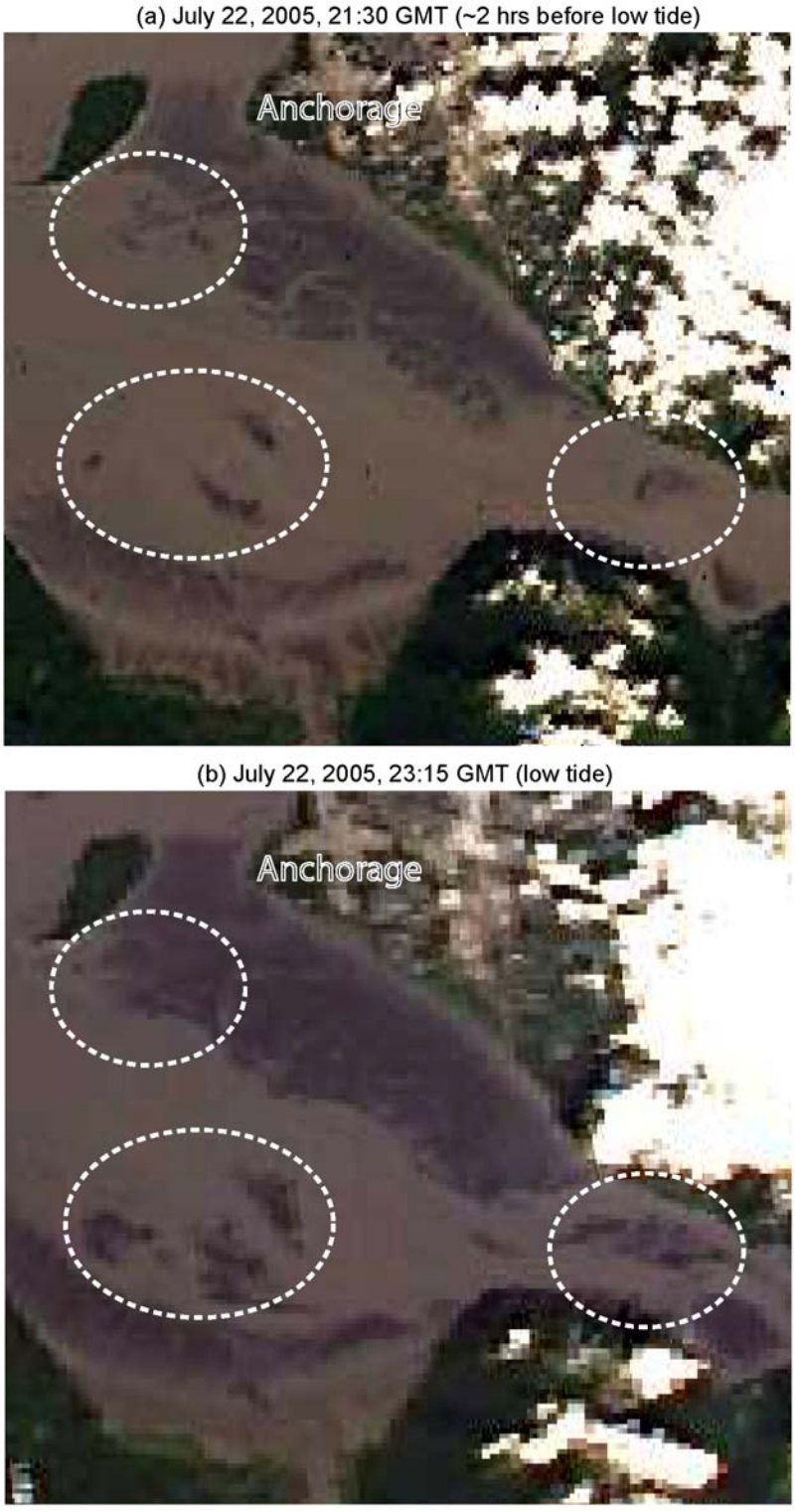

Fig. 9. Enlarged MODIS images in the region shown in Fig. 8a, for different times as indicated: (a) approximately 2 hours before low tide at Anchorage and (b) near low tide. These compare the changes (areas indicated by dashed ellipses) in mud flats exposure during the last 2 hours of low tide.

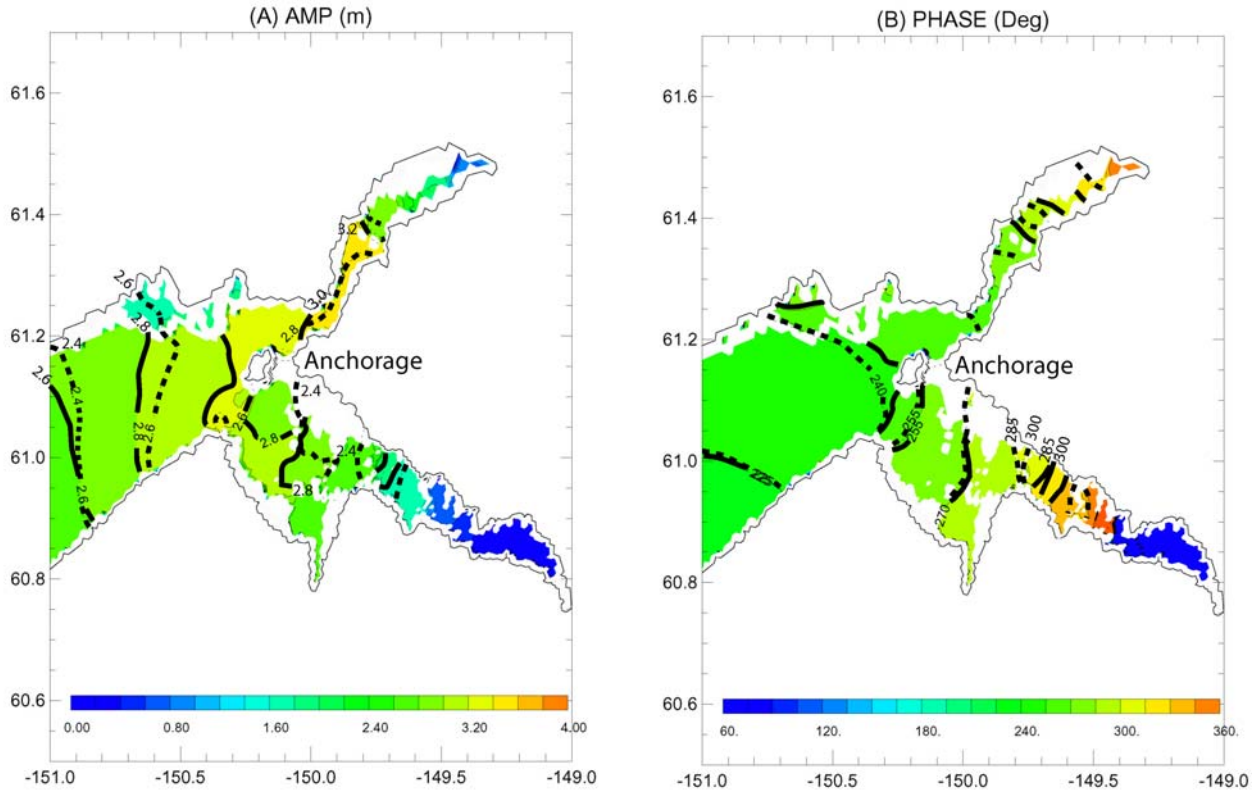

Fig. 10. Tidal (M2) amplitudes and phases for the experiment without WAD, 2Dpom (dashed contours) and with WAD, 2Dwad (solid contours; also color image) for the Upper Cook Inlet.

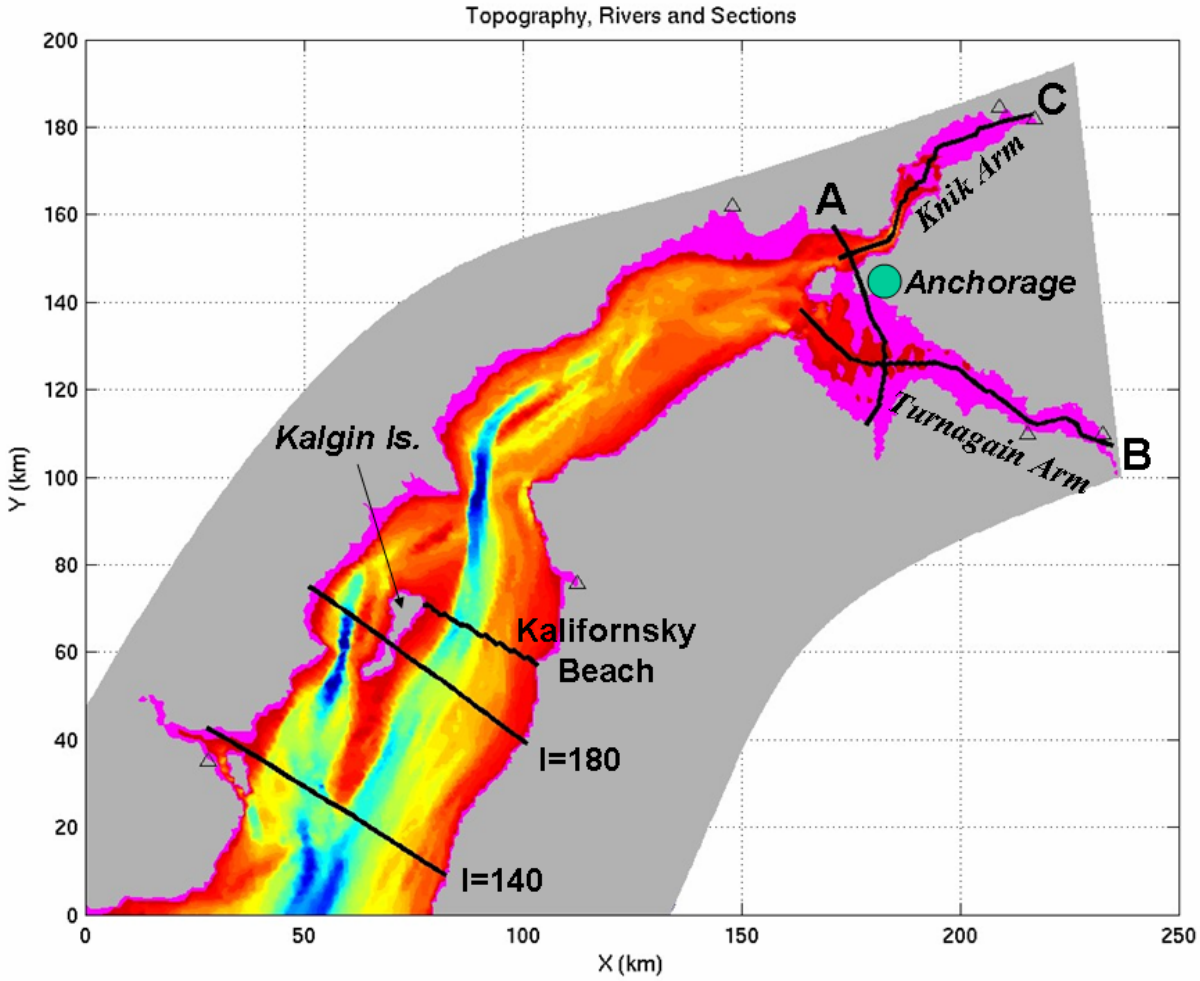

Fig. 11. Central and Upper Cook Inlet topography (color, scale is the same as in Fig.3) and locations of sections where various contours are plotted and discussed.

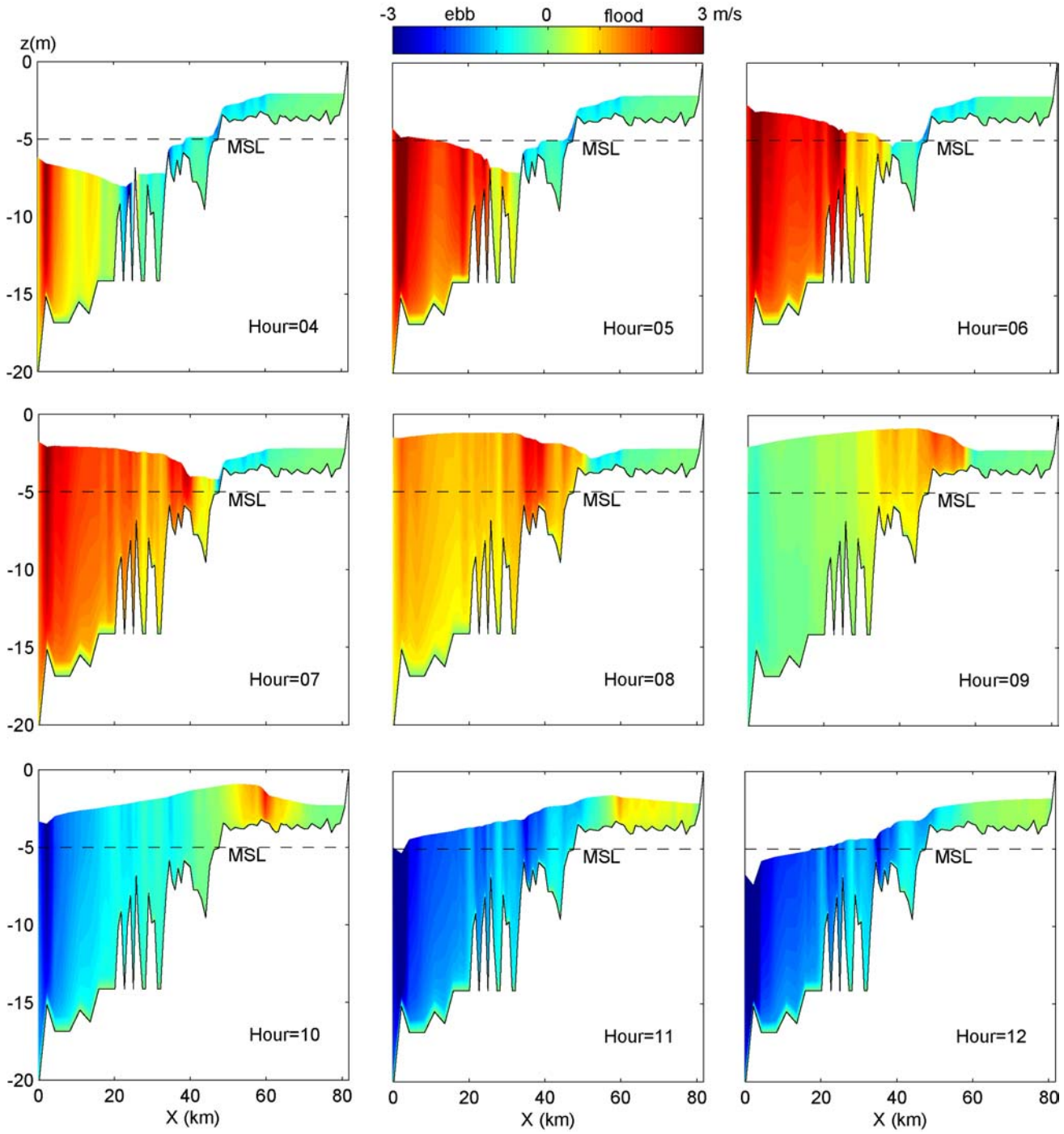

Fig. 12. Along-section velocity in Turnagain Arm (section B in Fig. 11). Shown are hourly plots starting 1 hour after the beginning of flood (Hour=04). Red indicates peak flood (i.e., southeastward flow toward the shallower region) and blue indicates peak ebb. The tidal elevation (m) is also shown and the mean sea level (MSL) is indicated.

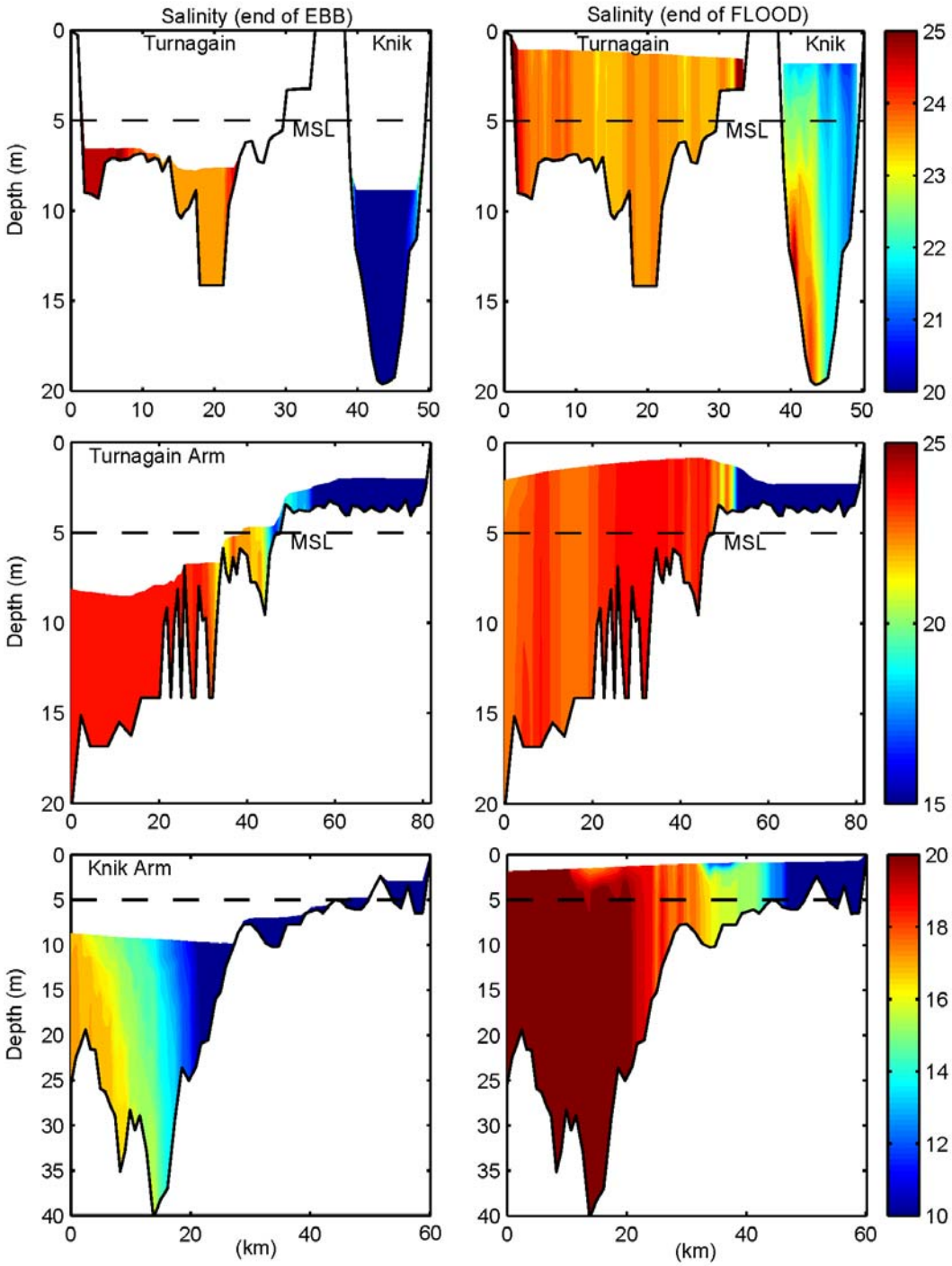

Fig. 13. Salinity in the three vertical sections shown in Fig. 11: A-section (upper panels), B-section (middle panels) and C-section (lower panels). Left panels are at low tide and right panels are at high tide.

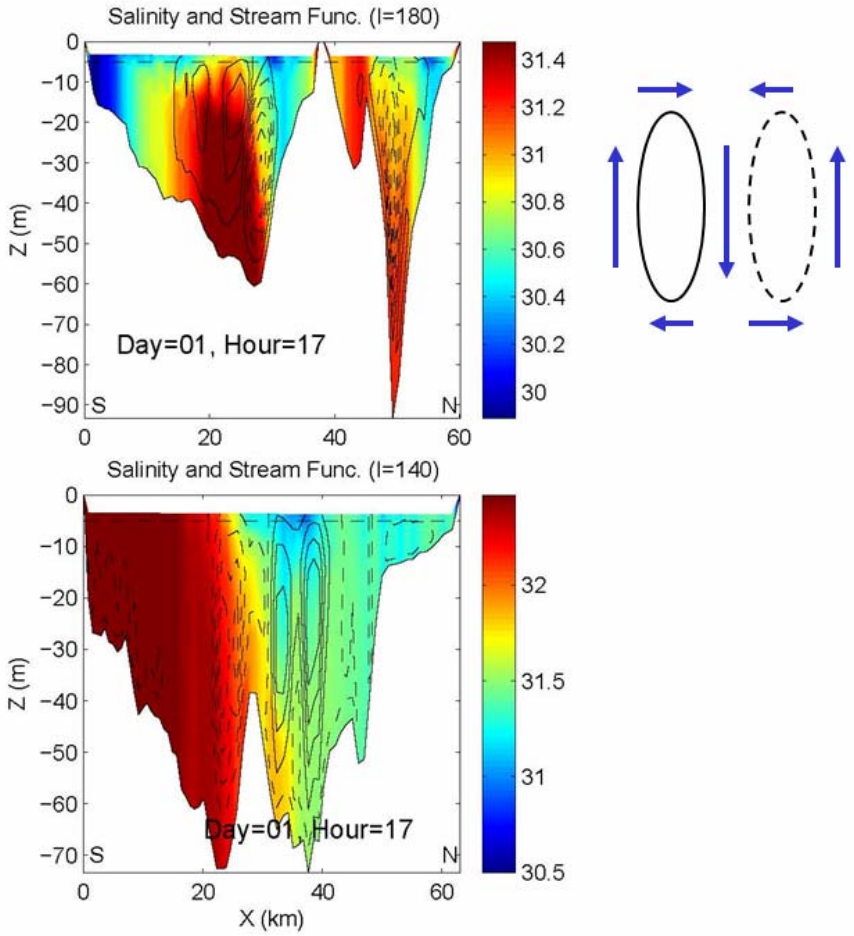

Fig. 14. Stream function (contours) and salinity (color) at one hour before peak (high) tide in the vertical sections "I=180" (upper panel) and "I=140" (lower panel) in the central Cook Inlet (see Fig. 11 for locations). The view is southwestward towards the Lower Inlet. Solid (dash) stream-function contours indicate clockwise (anti-clockwise) motion in the vertical plane as indicated in the inset. The stream function is calculated from the cross-channel components (V and W, see the corresponding velocity values in Fig. 15).

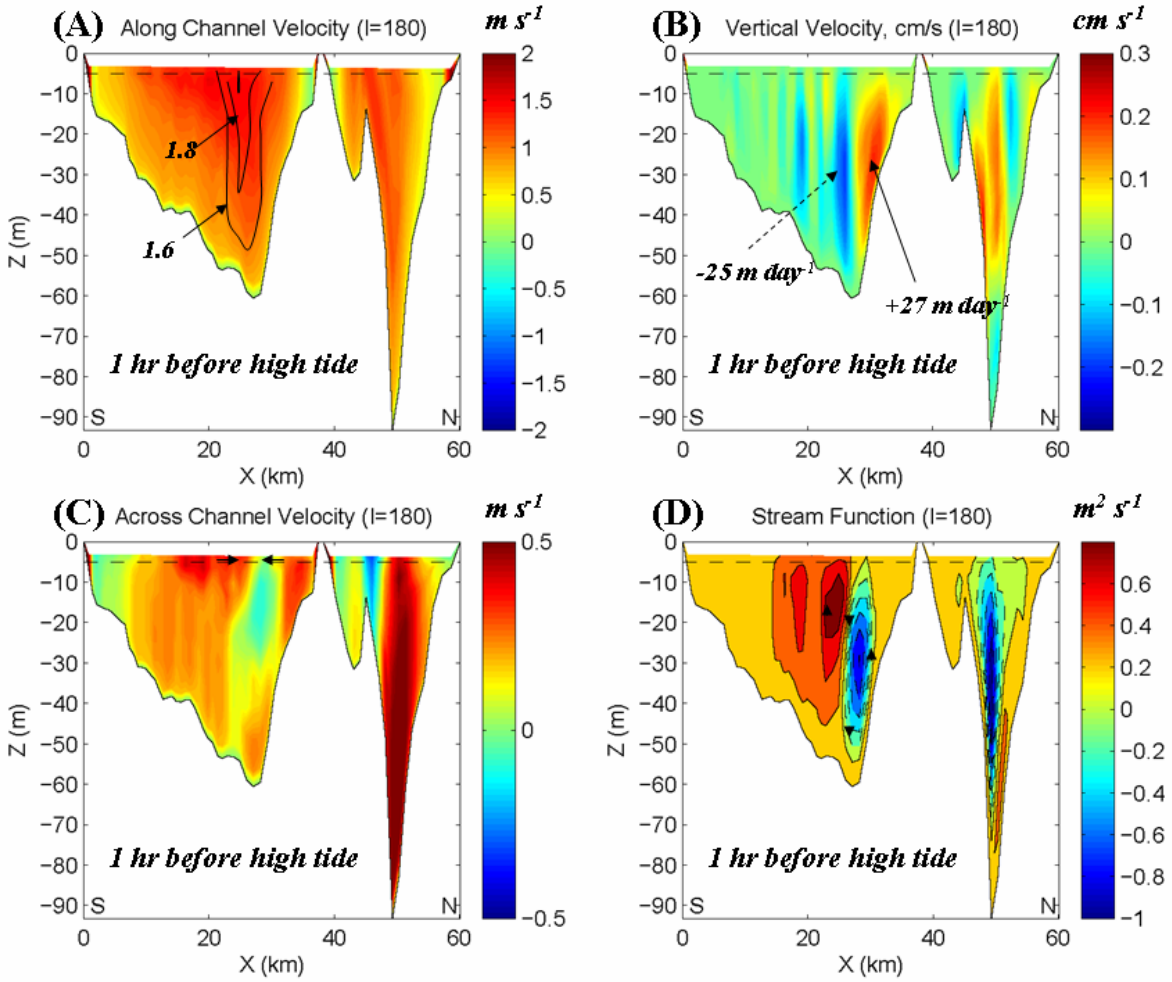

Fig. 15. Vertical-sectional contours of (A) U, (B) W, (C) V (across-section) and (D) stream function at the Kalgin Island section ("I=180"; see Fig. 11 for location).

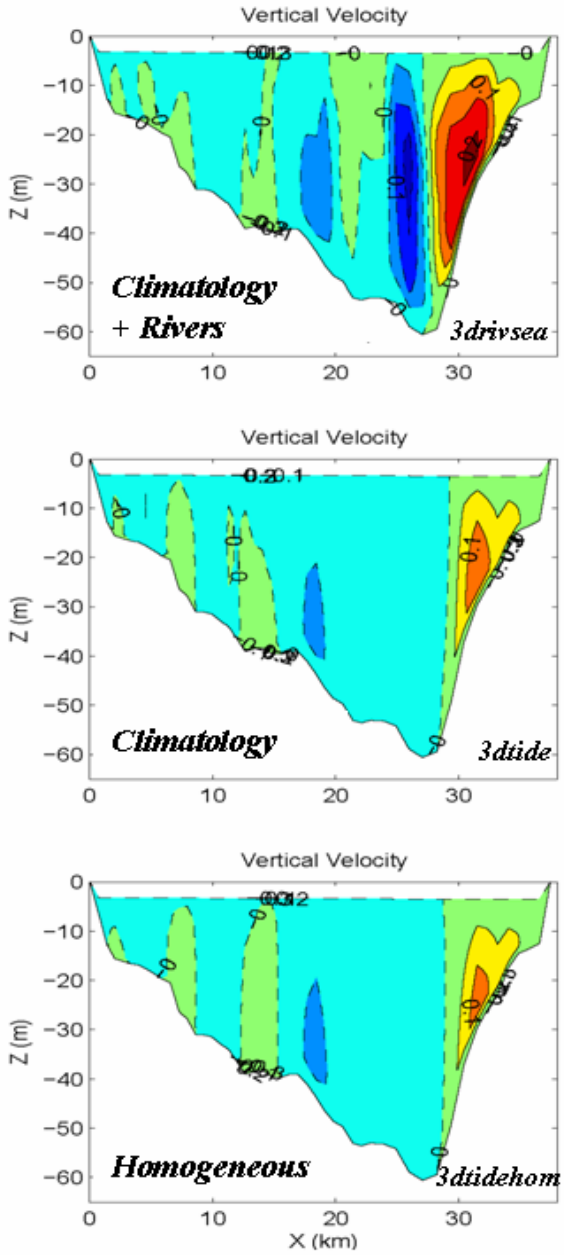

Fig. 16. Comparison of the vertical velocity contours at one hour before high tide at the Kalgin Island section ("I=180"; see Fig. 11 for location). For clarity, only the eastern portion of that section is shown. The three cases being compared are 3Drivsea, 3Dtide and 3Dtidehom (see Table 1 for details).

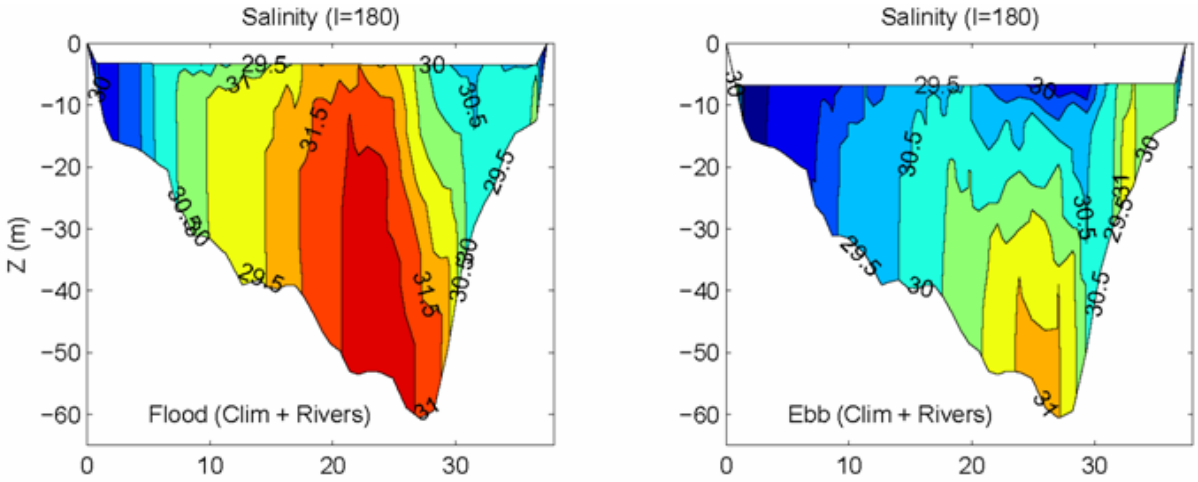

Fig. 17. Comparison of the vertical salinity contours at one hour before peak high tide (left panel) and one hour before peak ebb tide (right panel) at the Kalgin Island section ("I=180"; see Fig. 11 for location). For clarity, only the eastern portion of that section is shown. This case corresponds to Exp. 3Drivsea (see Table 1 for details).